Thermal Transport Mechanisms at Nanoscale Point Contacts

Li Shi

Arunava Majumdar
e-mail: majumdar@me.berkeley.edu

Department of Mechanical Engineering,
University of California,
Berkeley, CA 94720

We have experimentally investigated the heat transfer mechanisms at a 90±10 nm diameter point contact between a sample and a probe tip of a scanning thermal microscope (SThM). For large heated regions on the sample, air conduction is the dominant tip-sample heat transfer mechanism. For micro/nano devices with a submicron localized heated region, the air conduction contribution decreases, whereas conduction through the solid-solid contact and a liquid meniscus bridging the tip-sample junction become important, resulting in the sub-100 nm spatial resolution found in the SThM images. Using a one dimensional heat transfer model, we extracted from experimental data a liquid film thermal conductance of 6.7±1.5 nW/K. Solid-solid conduction increased linearly as contact force increased, with a contact conductance of 0.76±0.38 W/m^2-K-Pa, and saturated for contact forces larger than 38±11 nN. This is most likely due to the elastic-plastic contact between the sample and an asperity at the tip end.
[DOI: 10.1115/1.1447939]

Keywords: Contact Resistance, Heat Transfer, Microscale, Nanoscale, Probes

Introduction

The continuous scaling of semiconductor devices has produced devices with submicron feature sizes. Localized Joule heating in these devices is becoming a serious issue affecting device reliability. For example, current crowding and localized heating in deep submicron vias are known to strongly impact reliability of interconnects in very large-scale integrated (VLSI) circuits [1]. Experimental techniques for investigating thermal transport in semiconductor devices are needed for improving device design and for understanding device physics. Such techniques are also desirable for studying new thermophysical phenomena in nanoscale devices made of novel nanostructures, such as carbon electronics [2].

Scanning thermal microscopy (SThM) [3] has been developed to meet the need for thermally imaging devices and nanostructures. While the spatial resolution of other thermometry techniques based on far-field optics [4,5] are diffraction limited to the order of several microns, spatial resolution of 50 nm has been demonstrated for SThM [6].

A SThM operates by raster scanning a sharp temperature-sensing tip on a solid surface. The temperature-sensing tip is usually mounted on a micro cantilever of an atomic force microscope (AFM) probe so that tip-sample constant contact force is maintained by the force feedback loop of the AFM. While the tip scans on a sample, tip-sample heat transfer changes the tip temperature, which is measured and used to calculate the temperature or thermal properties of the sample at the tip-sample contact.

SThM has been used to locate ''hot spots'' in electronic devices and to image contrast in thermal properties of composite thin film materials [3]. In both cases, qualitative rather than quantitative results have been obtained. To accurately interpret a temperature map or a thermal property image obtained by SThM, a thorough understanding of heat transfer mechanisms at the tip-sample contact is required. The knowledge of heat transfer at micro or nanoscale contacts is, however, still limited [3,7,8]. Figure 1 shows the schematic diagram of a SThM tip in contact with a sample surface. Also shown are the various heat transfer mechanisms. The temperature sensor is a thin-film metal thermocouple junction fabricated at the end of the tip. The various tip-sample heat transfer mechanisms include solid-solid conduction at the contact, conduction through the air gap between the probe and the sample, radiation, and heat conduction through a liquid meniscus formed at the tip-sample junction. The liquid meniscus is formed from water molecules and/or contaminations adsorbed on the sample and tip surfaces. Luo et al. [7] speculated that conduction through the liquid meniscus could be the dominant heat transfer mechanism. This was used to explain the sub-100 nm spatial resolution obtained in the thermal image. Using a heated Pt wire probe to image thermal property contrast on a sample, Gomes et al. [8] recognized the importance of liquid-film conduction while suggesting that the predominant heat transfer mechanism depends on the sample thermal conductivity.

Recently, we have thermally designed and batch-fabricated SThM probes. Using these probes, we have thermally investigated localized heating in VLSI interconnects [9] and Joule heating in current-carrying carbon nanotubes [6] with a spatial resolution as small as 50 nm. Despite achieving sub-100 nm spatial resolution, there still remain questions regarding what is the dominant heat transfer mechanism in this nano-thermometry and what is the thermal contact resistance between the tip and the micro/nano structures. It is important to address these questions for quantitatively interpreting the thermal imaging results and for further improving the technique. In the following sections, we will (i) present several experiments for characterizing the heat transfer mechanisms at the nanoscale tip-sample point contact; (ii) describe a model considering various microscale heat transfer mechanisms for extracting point contact thermal resistance from the experimental data; and (iii) discuss the relative contribution of various conduction mechanisms under different conditions.

Experiments

Figure 2 shows the cross section and scanning electron micrographs of one of the thermal probes that we have thermally-designed and batch-fabricated [10]. The silicon nitride (SiN_x) cantilever was 128±1 μm long, 18.4±0.5 μm wide, and 0.89 ±0.01 μm thick. The tip was made of silicon dioxide (SiO_2), and was 8±0.5 μm high and the cone angle of the tip was 36 ±4 deg. Platinum (Pt) and chromium (Cr) films were sputtered and patterned on the cantilever and the tip. The thickness of each metal was 75±5 nm on the cantilever, as measured by AFM. Because of the steep slope of the tip, the metals deposited on the tip were much thinner, in the range of 20–25 nm for each metal as imaged by scanning electron microscopy (SEM). The two metals

Contributed by the Heat Transfer Division for publication in the JOURNAL OF HEAT TRANSFER. Manuscript received by the Heat Transfer Division February 8, 2001; revision received July 27, 2001. Associate Editor: D. Poulikakos.

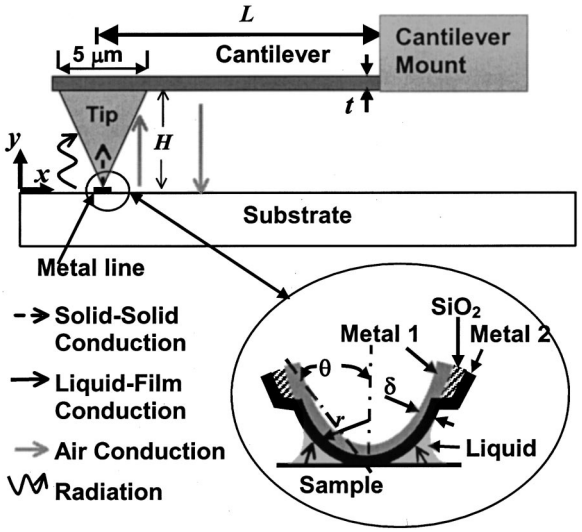

Fig. 1 Schematic diagram of a SThM probe in contact with a Joule heated metal line. Also shown are various tip-sample heat transfer mechanisms.

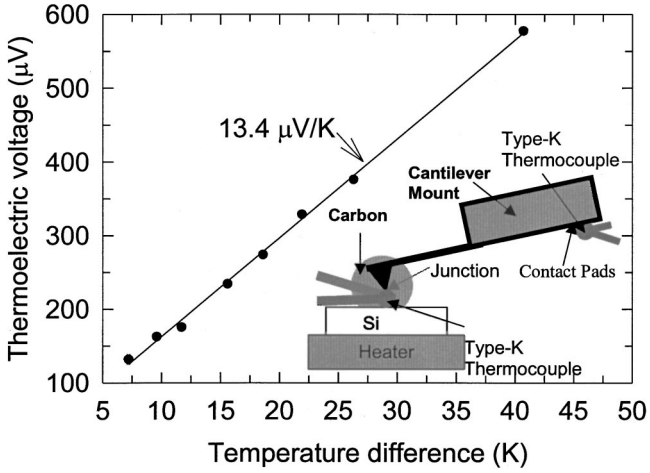

Fig. 3 Thermoelectric voltage as a function of temperature difference between the Pt-Cr junction and the contact pads. The inset shows the measurement setup

were separated by a 270 ± 10 nm thick SiO_2 film except at the very end of the tip. The junction at the tip end was 900 ± 60 nm high and 600 ± 30 nm wide at the base. The tip diameter was 90 ± 10 nm as measured by SEM. It should be noted that the cantilever design was not the optimized thermal design. However, because this probe has simpler geometry than other designs with cantilevers of *V* or other shapes, it is easier to model the heat transfer processes involved. Thus, this probe has been chosen for the following experiments.

We first measured the thermopower of the Pt-Cr junction using the experimental setup shown in the inset of Fig. 3. Under an optical microscope, a tiny drop of carbon paint was used to fix a probe tip to a fine Omega® type-K thermocouple mounted on a silicon substrate by silver paste. The tip was assumed to be at thermal equilibrium with the type-K thermocouple. Another type-K thermocouple was attached in close proximity to the Pt and Cr contact pads located at the end of the Pt and Cr lines. While the silicon substrate was heated to different temperatures, a thermoelectric voltage was created between the Pt and Cr contact pads due to the temperature difference between the Pt-Cr junction

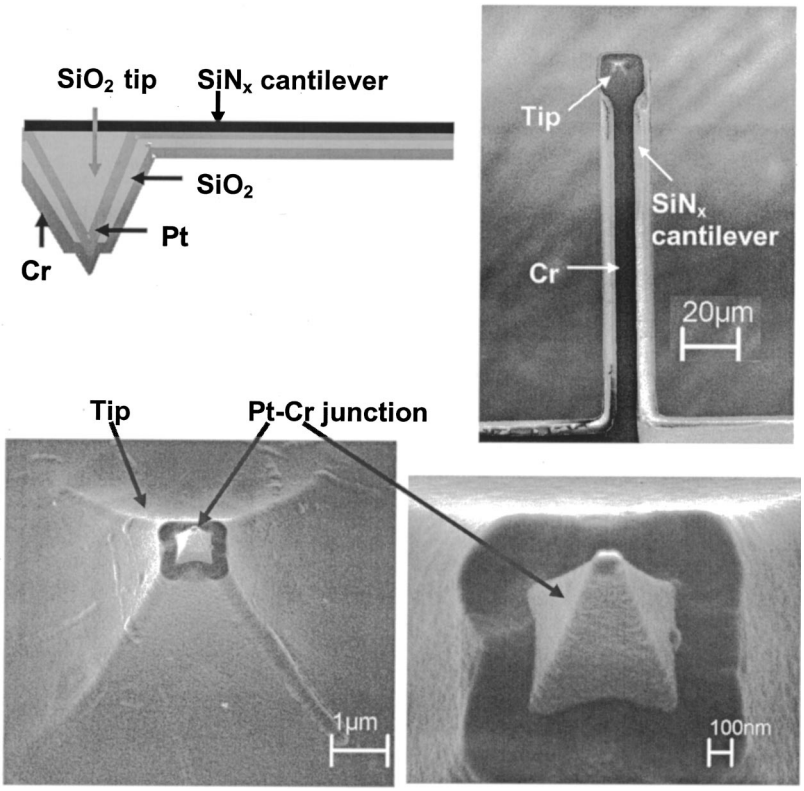

Fig. 2 Cross section (upper left) and scanning electron micrographs of a SThM probe (upper right), the probe tip (lower left), and the Pt-Cr junction (lower right) at the end of the tip

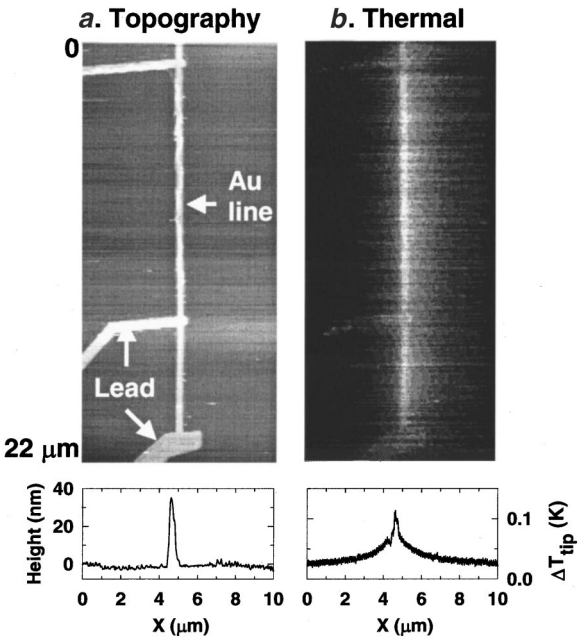

Fig. 4 Topographic (*a*) and thermal (*b*) images of a 350 nm wide Au line. One of the four leads to the Au line is located on top of the line and is not shown in the figure.

and the contact pads. This voltage was recorded as a function of the temperature difference between the two type-K thermocouples. From the same wafer containing the probe shown in Fig. 2, we chose a few probes for this destructive measurement. One of the measurement results is shown in Fig. 3. The thermopower of the Pt-Cr junction was found to be $13.4\pm0.06\ \mu$V/K, which is about half of that of a pure bulk Pt-Cr junction. Due to the thin-film confinement effect and differences in structure and purity, the thin metal films are expected to have different Seebeck coefficients as well as electrical and thermal conductivities from those of corresponding pure bulk metals.

The samples for studying tip-sample heat transfer were thin film metal lines with different line widths and lengths fabricated on silicon wafers containing a 1 μm thick SiO_2 film. The topographic image of a Au line obtained by the SThM probe is shown on Fig. 4(*a*). This particular sample was patterned using electron beam lithography and metal lift-off technique. The line was 350 ± 50 nm wide and 20 μm long. When a current passed between the two leads at the two ends of the line, the voltage drop at the middle segment was measured using the two middle leads that was 13 μm apart and was used to calculate the four-probe resistance. With a current of 1 μA, the resistance was measured while the sample was heated to different temperatures using a hot plate. From the resistance versus temperature curve shown in Fig. 5, we calculated the temperature coefficient of resistance (TCR) of the Au line to be $(152\pm0.6)\times10^{-6}\ \mathrm{K}^{-1}$. When the substrate was at room temperature and the line was Joule heated by a current in the range of 100–1500 μA, the temperature rise ΔT of the metal line can be determined as $\Delta T=(R-R_0)/(\mathrm{TCR}^*R_0)$, where R and R_0 are the four-probe electrical resistances when the line was Joule heated and at room temperature, respectively. The measured temperature rise, ΔT, is plotted as a function of current and is shown in Fig. 6.

When a current of $781.8\pm0.1\ \mu$A passed the Au line, a thermal image of the Joule heated line was obtained by the thermal probe, as shown in Fig. 4(*b*). During thermal imaging and all of the following experiments, the cantilever was parallel to the substrate and oriented perpendicular to the metal line. The thermal image shows that the temperature was uniform along the line. With the probe in contact with the heated metal line, we measured the

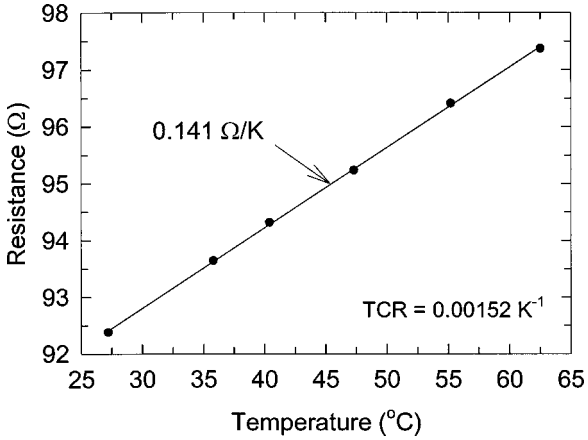

Fig. 5 Four-probe resistance of the Au line as a function of temperature

temperature response of the probe, which is defined as the ratio of the temperature rise at the Pt-Cr junction to that in the sample and has a unit of K/K. For the 350 nm wide line, the measured temperature response was only $0.05\pm0.01\ K/K$, as shown in Fig. 7. At first sight, this result surprised us because the temperature response of the probes were usually about 0.5 K/K when Al and Au metal lines with larger (3–50 μm) line widths were used to calibrate other probe designs [10], as shown in Table 1. To confirm that the low temperature response in Fig. 7 was not due to the specific design of the probe, we used the 350 nm wide line to

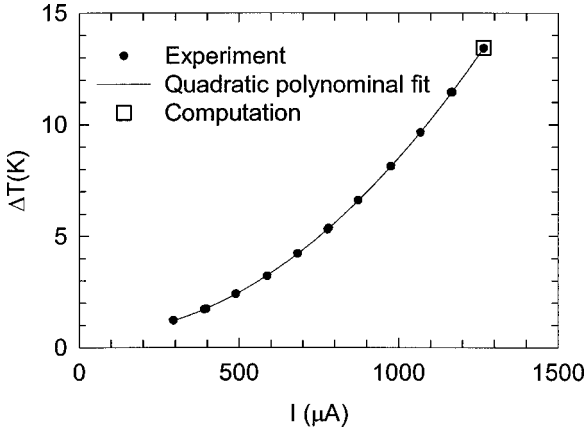

Fig. 6 Temperature of the Au line as a function of current

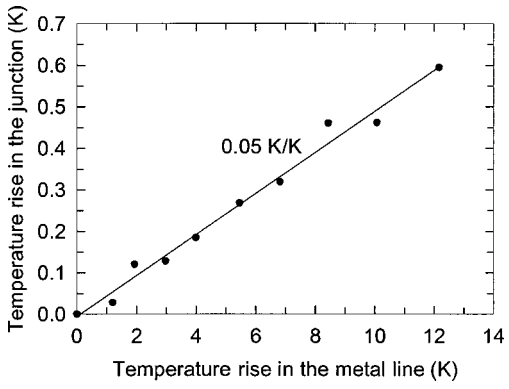

Fig. 7 Temperature rise in the Pt-Cr junction as a function of temperature rise in the 350 nm wide line in contact with the probe tip

Table 1 Temperature response of thermal probes with different dimensions on different samples. The cantilever is a V-shape. *L* is the cantilever length. *W* is the cantilever width and is expressed as two times the width of each of the two SiN_x arms. Cantilever thickness $t=0.89\pm0.01$ μm, tip height $H=8\pm0.5$ μm, Pt-Cr junction, junction height $h=900\pm60$ nm, thickness of each metal $=75\pm5$ nm, metal line width $w=5$ μm. The calibration samples were 2000 μm long Joule-heated thin film Al lines with different line widths.

Sample Line Width / Probe Dimension	3 μm	5 μm	50 μm
L = 100 μm, W = 2 x 8 μm	-	0.50±0.02	0.56±0.02
L = 100 μm, W = 2 x18 μm	-	0.50±0.02	-
L = 200 μm, W = 2 x 8 μm	0.46±0.02	-	0.53±0.02

measure the temperature responses of those probes used in Table 1 and obtained similar low temperature responses. The probe used for Fig. 7 was also calibrated with a 5.8 ± 0.2 μm wide, 45 ±5 nm thick, and 1500 μm long Joule heated Au line patterned on 1 μm thick oxide of a silicon wafer. As shown in Fig. 8, the measured temperature response was 0.64 ± 0.02 K/K, which was more than an order of magnitude larger than that for the 350 nm wide line.

Table 1 shows that the temperature response was larger for the 50 μm wide line than for the 3 μm wide line. This fact suggested that the probes was heated more by air conduction between the tip and the larger hot area for the 50 μm wide line than for the 3 μm one. Here, the much lower temperature response for the 350 nm wide Au line led us to suspect that air conduction might be responsible for the large temperature response obtained for the 5.8 μm wide lines.

To determine the relative contribution of various tip-sample heat transfer mechanisms, we Joule heated the 350 nm wide line to 5.3 ± 0.1 K above room temperature and recorded the cantilever deflection and probe temperature response simultaneously when the sample was raised toward and then retracted from the thermal probe. When the sample approached the tip, the cantilever deflection signal remained nearly zero before the sample contacted the tip, as shown in the deflection curve in Fig. 9. In this region, the temperature response was mostly due to air conduction between the probe and the sample, because radiation contribution is negligible when both the sample and the tip are close to room temperature [3]. As the tip-sample distance reduced, the temperature response due to air conduction increased slowly. Before the sample made solid-solid contact to the tip, the adsorbed liquid layers on the tip and the sample bridged each other. Initially, this liquid bridge pulled the tip down by van der Waals force, as being seen in the dip labeled as "jump to contact" in the deflection curve. Coincidentally, there was a small jump in the temperature response curve due to conduction through the liquid bridge. As the sample was raised further, both the solid-solid contact force and the temperature response increased gradually, until the cantilever deflection reached 100 nm higher than its previous position when the initial solid contact was just made. After this point, the temperature response remained almost constant as contact force increased.

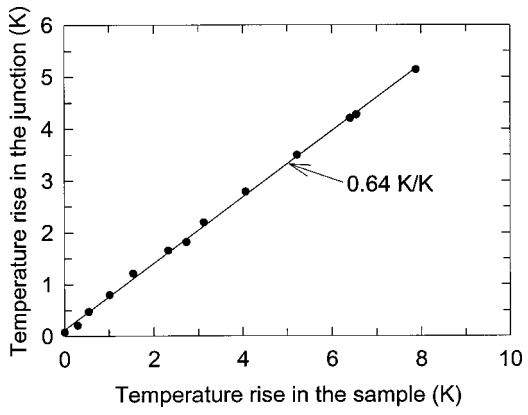

Fig. 8 Temperature rise in the Pt-Cr junction as a function of temperature rise in the 5.8 μm wide line in contact with the probe tip

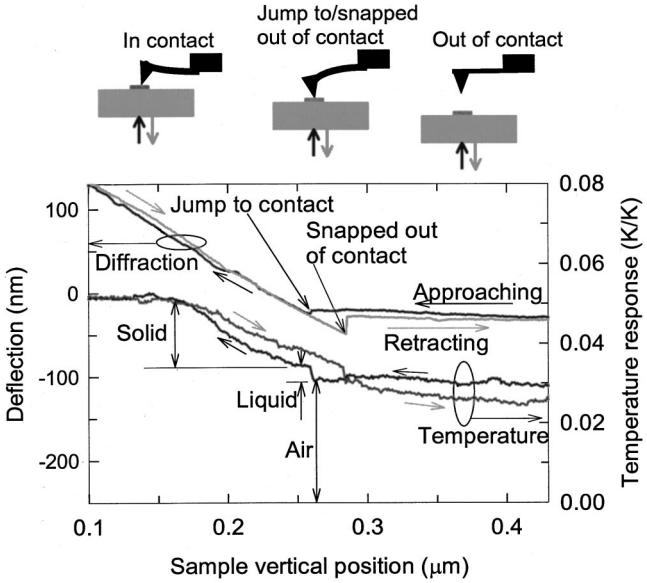

Fig. 9 Cantilever deflection and temperature response of the probe as a function of sample vertical position when the 350 nm wide line was raised toward and then retracted from the tip

As the sample was retracted from the tip, the temperature response again remained almost constant until at a cantilever deflection of 100 nm, the temperature response reduced roughly linearly but at a smaller slope than that found in the approaching cycle. As the sample was lowered further, the tip was pulled down together with the sample by surface tension of the liquid bridge until after a certain point, the restoring spring force of the cantilever exceeded the surface tension and the tip "snapped out of contact" with the sample. Associated with the breaking of the liquid bridge, there was a small drop in temperature response.

The above experiment shows several mechanisms. First, before tip-sample contact, air conduction contributed to a temperature response up to 0.03 K/K, which was about 60 percent of the maximum temperature response of 0.05 K/K at large contact force. Second, conduction through a liquid meniscus was responsible to the sudden jump and drop in temperature response when the tip "jumped to contact" to and "snapped out of contact" from the sample, respectively. Third, solid-solid conduction resulted in the almost linear increase or decrease of temperature response with contact force, which is a well understood feature for macroscopic solid-solid contacts [11]. Since the temperature response decreased at a slower slope during unloading (decreasing contact force), there must have been plastic deformation during loading (increasing contact force). For plastic deformation, contact area increases with load [12], resulting in the linear increase of solid-solid contact conductance with contact force. However, since the conductance was still a function of load during unloading, elastic recovery (spring back) must have been significant.

Besides the above-discussed hysteresis of temperature response

Table 2 Width, thickness, and Young's modulus of the four materials constituting the composite cantilever

Material	Width (μm)	Thickness (μm)	Young's modulus (GPa)
SiN_x	18.4 ± 0.5	0.89 ± 0.01	95 ± 10 (ref 14)
Pt	10 ± 0.5	0.075 ± 0.005	170 (ref 15)
SiO_2	18.4 ± 0.5	0.28 ± 0.2	57 ± 11 (ref 16)
Cr	7.7 ± 0.5	0.075 ± 0.005	140 (ref 15)

occurred during tip-sample contact, there was another hysteresis in the temperature response curve after the tip was released from the sample. As shown in Fig. 9, after the tip was snapped out of contact and when the substrate was retracted away from the tip, the temperature response was slightly different from those when the tip approached the sample at the same tip-sample distance. This indicates change in cantilever-sample heat transfer between approaching and retraction when tip and sample were out of contact. One possible scenario is that resonance vibration in the cantilever was excited after the tip was snapped out of contact with the sample. The vibration gave rise to convection and also change in air conduction between the cantilever and the sample, resulting in the hysteresis during approaching and retracting when tip was out of contact with the sample.

One question still remains as to why the temperature response saturated for cantilever deflection larger than 100 nm. To clarify this question, we first calculated the contact force corresponding to 100 nm deflection. The spring constant of the composite cantilever beam was calculated following Roark's formulas [13]. For a composite beam consisting of n different materials, the equivalent moment of inertia

$$I_{eq}=\sum_{i=1}^{n}\left(\frac{w_i^* t_i^3}{12}+w_i^* t_i^*(y_i-\bar{y})^2\right);\quad w_i^*=\frac{E_i}{E_1}w_i,$$

$$y_i=\frac{t_i}{2}+\sum_{j=i+1}^{n} t_k, \tag{1}$$

where w, t, and E are the width, thickness, and Young's Modulus. The centroidal axis

$$\bar{y}=\frac{\sum_{i=1}^{n} w_i^* t_i y_i}{\sum_{i=1}^{n} w_i^* t_i}. \tag{2}$$

The spring constant

$$K=\frac{E_1 I_{eq}}{L^3}, \tag{3}$$

where L is the cantilever length. Using the parameters listed in Table 2, we calculated $K=0.38\pm0.11$ N/m. Therefore, the 100 nm deflection corresponds to a contact force $F=38\pm11$ nN.

Assuming plastic deformation, this contact force resulted in a contact spot with a diameter

$$d_c=\sqrt{\frac{4F}{\pi H}}, \tag{4}$$

where H is the hardness of the tip or sample, whichever is softer. Among the tip and sample materials, the hardness of Au is the lowest [17]. For thin gold films, two measurement results for H were reported to be 500 MPa [18] and 1.5 GPa [19], respectively. For H on the order of 1 GPa, $d_c\approx8$ nm. As shown in Fig. 2, the tip diameter was about 90 nm. However, the details on the tip end

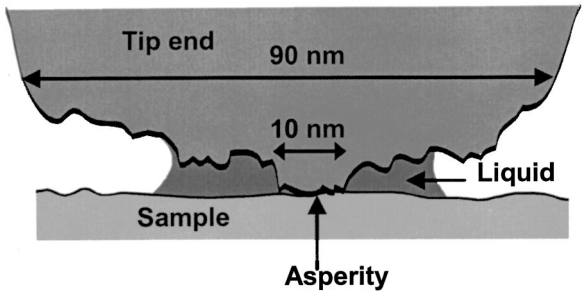

Fig. 10 A schematic diagram showing the contact between an asperity on the tip end and the sample

are not clearly shown in the SEM image due to the lack of resolution. We suspect that there were asperities of about 10 nm diameter on the tip end, as shown in Fig. 10. One of the asperities protruded out and first made contact with the sample. The linear increase in contact area is probably due to the roughness on the surfaces of the asperity and the sample, since it is well known that in the junction of random rough surfaces, the contact area increases linearly with contact force [20]. As the contact force increased to about 38 nN, the contact size approached the diameter of the asperity. At this point, the contact area could not increased further with contact force, until the asperity could be completely pressed into the soft sample by a contact force much larger than those used in the experiment. As a result, the temperature response in Fig. 9 remained almost constant for deflection larger than 100 nm. The feature, i.e., saturation of contact conductance at large contact forces, was not unique only to this particular thermal probe, but was also found for several other probes. Some of these probes had been used extensively for imaging before this force-calibration experiment, and it was possible that some of the asperities at the tip end have been worn out. For this case, another asperity could protrude out at the tip end and was responsible for the conductance saturation.

Now we will investigate why the temperature responses for the 5.8 μm wide heated line and the 350 nm one were so different. We repeated the point contact experiment for the 5.8 μm wide line and the result is plotted in Fig. 11. We can see that while the increase of temperature response due to solid and liquid conduction was similar in magnitude to that in Fig. 9, the temperature response due to air conduction, i.e., about 0.6 K/K, is one order of magnitude higher than the corresponding one (0.03 K/K) in Fig. 9.

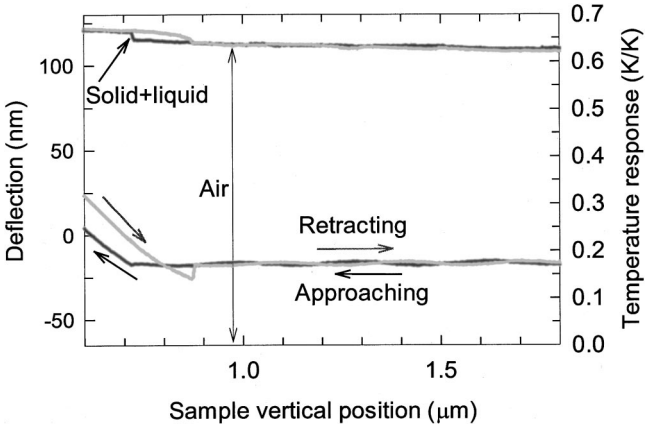

Fig. 11 Cantilever deflection and temperature response of the probe as a function of sample vertical position when the 5.8 μm wide line approached and then retracted from the tip

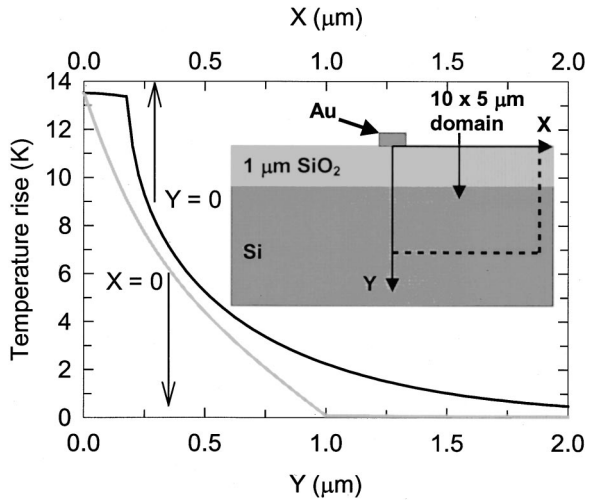

Fig. 12 Modeled temperature profile along the *X* and *Y* axis on the substrate of the 350 nm wide line. The inset shows the computation domain.

Therefore, it is clear that for the 5.8 μm wide line, air conduction dominated tip-sample conduction and is responsible for the large temperature response.

The above experiment reveals that the contribution of air conduction in tip-sample heat transfer depends on the size of the heated region on the sample. For larger heated regions, air conduction may dominate tip-sample heat transfer. As the characteristic size of the heat source reduces, the contribution of air conduction decreases and solid and liquid conduction become important. For micro/nano devices with localized submicron heated features, such as carbon nanotube circuits, air conduction contribution may reduce to a level smaller than that from solid-solid and liquid film conduction [6]. In the thermal images of these devices [6,9], the sub-100 nm resolution was a result of the increased contribution of local solid and liquid conduction; whereas, air contribution was insensitive to the distance between the tip and the heat source, giving rise to a slowly varying background signal.

Modeling

The purpose of the model is (i) to evaluate the thermal conductance of the liquid meniscus, and that of the solid-solid contact; and (ii) to examine the possible deviation of SThM-measured temperature profiles from the true ones due to the influence of air conduction. To do this, it is necessary to calculate the temperature response of the probe for different tip-sample distance. In the calculation, it was assumed that the temperature was constant at each horizontal cross sections of the tip and only varied along the height or y direction, as shown in Fig. 1. This assumption can be justified because the external thermal resistance through the air is much larger than the internal thermal resistance in the tip across each horizontal cross section. Although Fig. 1 shows that the tip is in contact with the sample, we consider a general case that the tip end is at a distance d above the sample. Tip-sample contact corresponds to $d \leq 0$. In addition, y is measured from the end of the tip instead of from the sample surface.

The sample was the 350 nm wide Au line Joule heated to a temperature T_s. The resulting temperature profile on the SiO_2 substrate surface was calculated using a finite difference method. It was assumed that the temperature does not change along the length of the metal line, yielding a two-dimensional problem. This assumption can be justified by the SThM image in Fig. 4(b) and is expected because the length of the line (20 μm) was much larger than the thickness (1 μm) of the SiO_2 film. We considered a computation domain of $0 \leq X \leq 10$ μm and $0 \leq Y \leq 5$ μm, as shown in the inset of Fig. 12. The temperature rise sufficiently far away at $X = 10$ μm and $Y = 5$ μm is assumed to be zero. We ignored heat dissipation through the air and assumed an adiabatic boundary condition on the sample surface. The symmetric geometry results in an adiabatic boundary condition at $X = 0$. For a grid size of 25 nm by 25 nm, we solved the temperature distribution in the computation domain for an electrical current of 1267 μA flowing in the line. We confirmed that the modeled temperature profile did not change when the grid size was increased by a factor of 2. The temperature profile on the top surface, i.e., $Y = 0$, and that of $X = 0$ are plotted in Fig. 12. The average temperature rise of the Au line was calculated to be 13.45 K, which agrees well with the measurement result of 13.42 K obtained from Fig. 6. The temperature decays to almost room temperature at the SiO_2 and Si interface, which is expected because of the high thermal conductivity of Si compared to that of SiO_2 (see Table 3). The temperature also approaches room temperature for $X > 2$ μm. The modeling results, hence, justify the assumption that temperature rise is zero at $X = 10$ μm or $Y = 5$ μm.

Table 3 Thermophysical properties of candidate probe materials

	Thermal Conductivity at 300 K (W/m-K) (ref. 21)
Cr	93.7
Pt	71.6
Si	148
SiO_2	1.4
SiN_x	5.5 (ref. 22)

With the known temperature profile on the substrate, the one-dimensional heat conduction equation in the tip can be written as

$$\frac{d}{dy}\left[(A_t(y)k_t(y)+A_m k_m)\frac{dT(y)}{dy}\right]-p(y)h_a(y)\tan\theta(T(y)-T_{\text{sub}}(y))=0. \quad (5)$$

Here, θ and r are the half angle and the radius of the conical tip, respectively, as shown in Fig. 1, A_t and k_t are the cross section area and thermal conductivity of the SiO_2 tip, respectively, k_m and A_m are the cross section area and thermal conductivity of the metal coating on the tip, respectively, and p is the perimeter of the square cross section of the tip. For each point on the perimeter, we assumed that heat was conducted by air between this point and a point right below on the substrate, and treated these two points as two parallel plates. This simplified picture of tip-sample air conduction is represented by the second term in Eq. (5), where T_{sub} was the temperature of the point on the substrate. The distance between the two points on the tip and substrate, respectively, is $y+d$. The air conduction coefficient h_a needs to be written in different forms for different values of $(y+d)/\lambda$, where λ is the mean free path of air molecules and is about 60 nm under ambient condition and at sea level [23]. For $(y+d)/\lambda > 100$, we assumed a constant temperature gradient at the air gap and used $h_a = \alpha k_a/(y+d)$, where k_a is the thermal conductivity of bulk air and α is a geometry factor to accommodate the fact that the tip and the substrate is not exactly two parallel plates. We will obtain α by fitting the modeling results with measurement data. For $1 < (y+d)/\lambda < 100$, significant temperature discontinuity may develop at the air-solid boundaries because intermolecular collisions

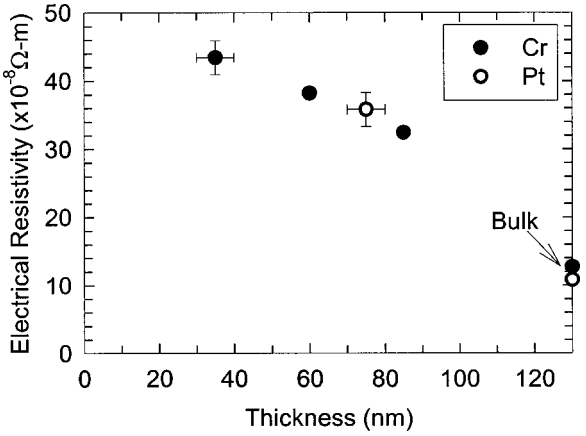

Fig. 13 Electrical resistivity as a function of the thickness of the Pt and Cr films

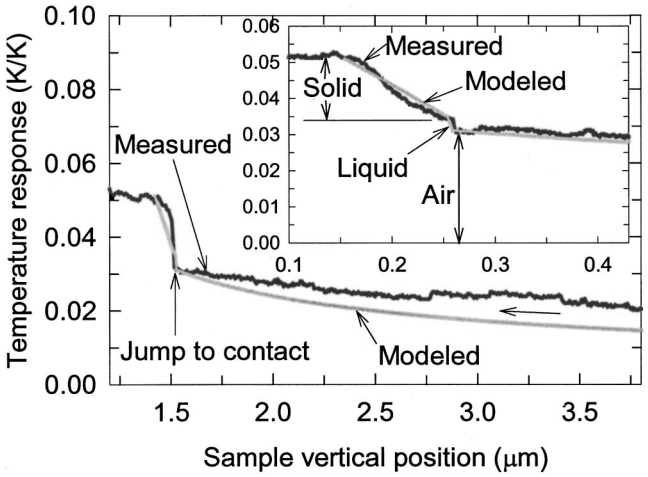

Fig. 14 Modeled and measured temperature responses of the probe as a function of sample vertical position when the 350 nm wide line approached the tip

become less frequent and molecules arriving at the solid surfaces are unable to come into equilibrium with the surface [23]. In this so-called slip regime,

$$h_a=\frac{\alpha k_a/(y+d)}{1+2\,f\lambda/(y+d)};\quad f=\frac{2(2-A)\gamma}{A(\gamma+1)\mathrm{Pr}},\tag{6}$$

where A is a thermal accommodation coefficient and is about 0.9 for air, γ is the ratio of air heat capacity, and Pr is the Prandtl number. For $(y+d)/\lambda<1$,

$$h_a=\frac{\alpha k_a'}{(y+d)(1+2\,f)};\quad k_a'=CV(y+d)/3,\tag{7}$$

where k_a' is the thermal conductivity of air in the free molecule flow regime, and C and V is the heat capacity and velocity of air molecules, respectively.

The boundary conditions are

$$(A_t k_t+A_m k_m)\frac{dT}{dy}=\frac{T-T_s}{R_{ts}},\quad \text{at}\quad y=0\tag{8a}$$

$$(A_t k_t+A_m k_m)\frac{dT}{dy}=\frac{T_0-T}{R_c},\quad \text{at}\quad y=H,\tag{8b}$$

where R_{ts} is the tip-sample thermal resistance. When the tip is not in contact with the sample, $R_{ts}=[h_a(A_t+A_m)]^{-1}|_{y=0}$, as a result of air conduction between the tip end and the sample. When the tip was in contact with the sample, or $d\leqslant 0$, R_{ts} is due to solid-solid and liquid film conduction and will be obtained by fitting the modeling result with measurement data. T_0 is the ambient temperature.

When the cantilever was oriented perpendicular to the 350 nm wide metal line with the tip above the center of the line, the substrate right below the cantilever arm was more than 2.5 μm away from the metal line, because the base of the tip was 5 μm wide, as shown in Fig. 1. For the 350 nm wide line, the substrate temperature approaches room temperature for $X>2$ μm, as shown in Fig. 12. Accounting for air conduction between the cantilever and the room temperature substrate below, the thermal resistance of the cantilever, R_c is solved using fin theory [24]

$$R_c=\frac{\tanh(mL)}{mk_c wt};\quad m=\sqrt{\frac{h_a}{k_c t}},\tag{9}$$

where L, w, t, and k_c are the length, width, thickness, and thermal conductivity of the cantilever, respectively, h_a is the heat conduction coefficient of the air gap between the cantilever and the substrate and was calculated following the discussion in the preceding paragraph with $\alpha=1$ because the cantilever and the substrate can be treated as two parallel plates.

The thermophysical properties of candidate probe materials are tabulated in Table 3, where the thermal conductivity data of the metals are for pure bulk metals. To determine the thermal conductivities of the thin metal films, we measured their electrical conductivities as a function of thickness, as shown in Fig. 13. Using Wiedemann-Franz law and assuming that the reduced thermal conductivities of the thin metal films had the same proportionality with the reduced electrical conductivities [25], we estimated the thermal conductivities of the thin metal films on the cantilever. From the electrical conductivity measurements, the correction factors with respect to bulk values were 0.3 for Pt and 0.39 for Cr. For the even thinner metals on the tip, the correction factor were 0.22 for Pt and 0.28 for Cr. It is unnecessary to correct the thermal conductivity of SiO_2 at the SiO_2 tip end, because the phonon mean free path in amorphous SiO_2 is expected to be shorter than the size of the end of the SiO_2 tip [26], which was about 20 nm.

Equation (5) was solved using a finite difference method to obtain the temperature distribution in the tip, i.e., $T(y)$, for different value of tip-sample distance d. A non-dimensional temperature at a distance y away from the sample was defined as

$$\phi(y)=\frac{T(y)-T_0}{T_s-T_0}.\tag{10}$$

Due to the particular geometry of the junction at the tip end, the measured thermal signal corresponds to the temperature difference between the room temperature and that at about 900 nm away from the tip end for the probe shown in Fig. 2. We plotted the modeled temperature response $\phi(y=900\,\mathrm{nm})$ as a function of tip-sample distance in Fig. 14. Two measurement results are also shown in Fig. 14. The sample travelling range was 0.5 μm for the measurement result in the inset and 3.8 μm for the other one. For the one with 3.8 μm travelling range, the distinction between the sudden jump due to liquid conduction and the gradual increase due to solid-solid conduction is unclear due to the lack of resolution in sample position. To fit the modeling results with the experimental ones while the tip was not in contact with the sample, we used $\alpha=0.8$ to correct tip-sample air conduction for the deviation from that between two parallel plates. Considering the 0.01 K/K uncertainty in the measured temperature response, we estimated the uncertainty in α to be ± 0.1. After obtaining α, we used $R_{ts}=(1.5\pm 0.3)\times 10^8$ K/W to fit the magnitude of the temperature jump due to liquid film conduction. This resistance value corresponds to a liquid film thermal conductance $G_{lf}=6.7\pm 1.5$ nW/K. To fit the modeling result with the measured saturated value of temperature response at the critical contact force

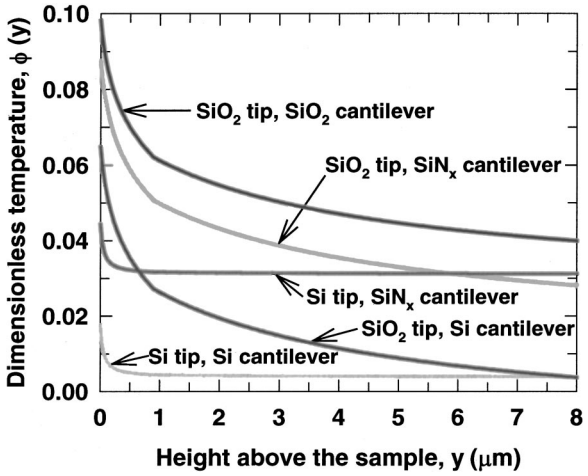

Fig. 15 Temperature in the tip as a function of *y* for different tip and cantilever materials

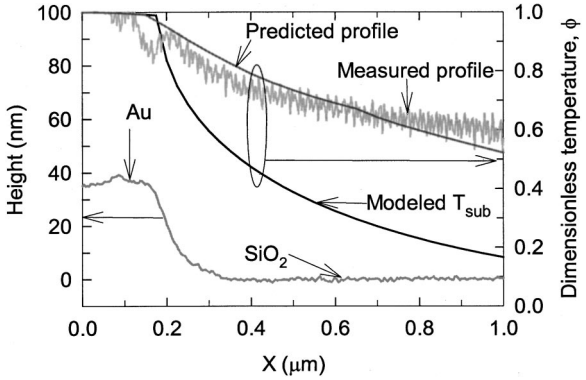

Fig. 16 Modeled temperature profile, predicted SThM-measured temperature and actual SThM measured temperature and height profiles across the 350 nm wide line

$F=38\pm11$ nN, we used a solid-solid contact conductance of $G_{ss}=(29\pm6)$ nW/K, assuming that liquid film conductance did not change for contact forces smaller than 38 ± 11 nN. Therefore, the proportionality between solid-solid contact thermal conductance and contact pressure is $G_{ss}/F=0.76\pm0.38$ W/m^2-K-Pa.

The estimated liquid and solid-solid conductances are different from what were suggested by previous work [7]. In that work, the solid-solid conductance was estimated to be on the order of 10–100 nW/K, which was close to what was found in this work. However, the liquid film conductance was estimated to be on the order of 1 μW/K, two orders of magnitude larger than the current result. The estimation of liquid film conductance did not include the contact conductance at the solid-liquid interfaces, which may be much lower than the conductance through the liquid film of monolayer thickness. Therefore, the liquid film conductance could be quite low, as found in this study.

The low solid-solid and liquid-solid contact conductance results in low temperature responses for samples with a localized submicron heated region, such as the 350 nm wide line as well as defective submicron VLSI vias or current carrying-carbon nanotubes. To improve the temperature response, there is still some room to improve regarding the thermal design of the probes. In fact, the current probes made of low-thermal conductivity materials was expected to have larger temperature response than those constructed from high-thermal conductivity ones. To confirm this, we calculated the temperature response of the probe for different probe materials. For a liquid film conductance $G_{lf}=6.7$ nW/K and a maximum solid-solid contact conductance $G_{ss}=29$ nW/K, the temperature distribution in the tip is calculated for different combinations of tip and cantilever materials and is plotted in Fig. 15. Clearly, the temperature response of the probe is improved for using low thermal conductivity materials such as SiN_x and SiO_2. The temperature response can be further improved for smaller (100–300 nm high) junctions and narrower cantilever width, etc, as discussed in another paper [10].

Last, due to the influence of air conduction, the measured temperature profile may deviate from the true one. This may occur even when air conduction contribution decreases for the 350 nm wide line and other micro/nano devices with submicron localized heated features. Using the above model with $G_{lf}=6.7$ nW/K, and a solid-solid conductance $G_{ss}=14.5$ nW/K corresponding to 50 nm cantilever deflection, and $\alpha=0.8$, we predicted that the SThM-obtained temperature profile across the 350 nm wide line decays slower than the true substrate temperature shown in Fig. 12. The predicted SThM measurement result and the substrate temperature profile from Fig. 12 are plotted in Fig. 16. For the ease of comparison, we plotted a dimensionless temperature ϕ defined as $\phi=\Delta T(X)/\Delta T(0)$, where $\Delta T(X)$ is the temperature rise of the sample surface at a distance X away from the center of the Au line. To confirm the prediction, the SThM-measured temperature and height profiles are also shown in Fig. 16. Note that the cantilever deflection was maintained at 50 nm during tip scanning. Figure 16 shows that the measurement result agrees well with the prediction. This confirms that the modeling results of G_{lf}, G_{ss}, and α are in the correct ranges. Furthermore, the results in Fig. 16 suggest that it is desirable to perform SThM at vacuum, as has been demonstrated by Nakabeppu et al., [27], in order to eliminate the unwanted influence of air conduction.

Conclusion

We have experimentally investigated the heat transfer mechanisms at the SThM tip-sample contact with a contact diameter of 90 ± 10 nm. The contribution of tip-sample air conduction depends on the size of the heated region on the sample and is not sensitive to tip-heat source distance. For large heated regions, air conduction dominates tip-sample heat transfer, resulting in large temperature responses. For micro/nano devices with submicron localized heated region, the contribution of air conduction decreases; whereas, conduction through the solid-solid contact and a liquid meniscus become important, resulting in sub-100 nm spatial resolutions achieved in SThM images. Despite the superior spatial resolution, SThM-measured temperature profiles deviate from the true one due to the influence of air conduction. Therefore, it is desirable to perform SThM in vacuum to eliminate the unwanted influence of air conduction.

To estimate the magnitude of solid-solid and liquid film conductance, we developed a one-dimensional heat conduction model considering various microscale heat transfer mechanisms. Using the model, we inferred from the experimental data that the thermal conductance of the liquid meniscus was $G_{lf}=6.7\pm1.5$ nW/K. Solid-solid conduction increased linearly with the contact force with a contact conductance of 0.76 ± 0.38 W/m^2-K-Pa. For contact forces larger than 38 ± 11 nN, solid-solid conductance saturated. This is most likely because at large contact forces, the contact size between the sample and an asperity on the tip end approached the asperity diameter of about 10 nm, and could not increased further with contact force.

Acknowledgment

The authors thank DOE (Engineering Division, Basic Engineering Sciences) and NSF (Chemical and Transport Systems) for providing financial support for this work.

Nomenclature

A = thermal accommodation factor for air conduction when the length scale is close to the mean free path of air molecules
C = specific heat of air (W/kg-K)
d = contact diameter (m) or tip-sample distance (m)
G = thermal conductance (W/K)
h = air conduction coefficient (W/m^2-K)
H = height of the tip (m) or hardness (Pa)
I = current (A)
k = thermal conductivity (W/m-K)
K = spring constant (N/m)
L = length of the cantilever (m)
n = number of materials of the composite cantilever
p = perimeter of a horizontal cross section of the tip (m)
r = tip radius (m)
R = thermal or electrical resistance (K/W or Ω)
t = cantilever thickness (m)
T = temperature (K)
V = velocity of air molecules
W = cantilever width (m)
x, X, y, Y = coordinate (m)

Greek Letters

α = correction factor for air conduction between the tip and sample
δ = thickness of the metal film (m)
ΔT = temperature rise (K)
ϕ = dimensionless temperature
λ = mean free path of air molecules (m)
θ = half angle of the conical tip (°)

Subscripts

a = air
c = cantilever or contact
lf = liquid film
m = metal film
t = tip
ts = tip to sample
s = sample
ss = solid-solid
0 = ambient condition

References

[1] Kwok, T., Nguyen, T., Ho, P., and Yip, S., 1987, "Current Density and Temperature Distributions in Multilevel Interconnections With Studs and Vias," IEEE Proc. Int. Reliab. Phys. Symp., **25**, pp. 130–135.
[2] Dekker, C., 1999, "Carbon Nanotubes as Molecular Quantum Wires," Phys. Today, **52**, No. 5, pp. 22–8.
[3] Majumdar, A., 1999, "Scanning Thermal Microscopy," Annu. Rev. Mater. Sci., **29**, pp. 505–585.
[4] Khurana, N., and Chiang, C.-L., 1986, "Analysis of Product Hot Electron Problems by Gated Emission Microscopy," IEEE Proc. Int. Reliab. Physics Symp., **25**, pp. 189–194.
[5] Ju, Y. S., and Goodson, K. E., 1998, "Short-Time-Scale Thermal Mapping of Micro Devices Using a Scanning Thermoreflectance Technique," ASME J. Heat Transfer, **120**, No. 2, pp. 306–313.
[6] Shi, L., Plyasunov, S., Bachtold, A., McEuen, P. L., and Majumdar, A., 2000, "Scanning Thermal Microscopy of Carbon Nanotubes using Batch Fabricated Probes," Appl. Phys. Lett., **77**, No. 26, pp. 4295–4297.
[7] Luo, K., Shi, Z., Varesi, J., and Majumdar, A., 1997, "Sensor Nanofabrication, Performance, and Conduction Mechanisms in Scanning Thermal Microscopy," J. Vac. Sci. Technol. B, **15**, No. 2, pp. 349–360.
[8] Gomes, S., Trannoy, N., and Grossel, P., 1999, "DC Thermal Microscopy: Study of the Thermal Exchange Between a Probe and a Sample," Meas. Sci. Technol., **10**, pp. 805–811.
[9] Shi, L., Kwon, O., Wu, G., and Majumdar, A., 2000, "Quantitative Thermal Probing of Devices at Sub-100 nm Resolution," IEEE Proc. Int. Reliab. Phys. Symp., **38**, pp. 394–398.
[10] Shi, L., Kwon, O., Miner, A., and Majumdar, A., 2001, "Design and Batch Fabrication of Probes for Sub-100 nm Scanning Thermal Microscopy," J. Microelectromech. Syst., **10**, pp. 370–378.
[11] Williamson, M., and Majumdar, A., 1992, "Effect of Surface Deformations on Contact Conductance," ASME J. Heat Transfer, **114**, pp. 802–810.
[12] Johnson, K. L., 1985, *Contact Mechanics*, Cambridge University Press, NY.
[13] Roark, R. J., and Young, W. C., 1989, *Roark's Formulas for Stress and Strain*, McGraw-Hill, NY.
[14] Kiesewetter, L., Zhang, J.-M., Houdeau, D., and Steckenborn, A., 1992, "Determination of Young's Moduli of Micromechanical Thin Films Using the Resonance Method," Sens. Actuators A, **35**, pp. 153–159.
[15] Helg, B., 1990, "On a Nonvolatile Memory Cell Based on Micro-Electro-Mechanics," IEEE Proc. Micro Electro Mechanical Systems, Napa Valley, CA., **90**, pp. 172–176.
[16] Peterson, K. E., 1978, "Dynamic Micromechanics on Silicon: Techniques and Devices," IEEE Trans. Electron Devices, **ED25**, pp. 1241–1250.
[17] Samsonov, G. V., ed., 1968, *Handbook of the Physicochemical Properties of the Elements*, IFI-Plenum, New York.
[18] Insepov, Z., Manory, R., Matso, J., Yamada, I., 1999, "Ionized Cluster Beam as a Hardness Measurement Tool," Nucl. Instrum. Methods Phys. Res. B, **148**, pp. 47–52.
[19] Jiang, D. S., and Kim, D. E., 1996, "Tribological Behavior of Ultra-Thin Soft Metallic Deposits on Hard Substrate," Wear, **196**, pp. 171–179.
[20] Cooper, M. G., Mikic, B. B., and Yovanovich, M. M., 1969, "Thermal Contact Conductance," Int. J. Heat Mass Transf., **12**, pp. 279–300.
[21] Touloukian, Y. S., and Ho, C. Y., 1972, *Thermophysical Properties of Matter*, Vols. 1 and 2, Plenum Press, New York.
[22] The thermal conductivity of low stress SiN_x was measured by S. Huxtable in our group using the 3-ω method.
[23] Rohsenow, W., and Choi, H., 1961, *Heat, Mass, and Momentum Transfer*, Prentice-Hall, Englewood Cliffs, NJ.
[24] Bejan, A., 1993, *Heat Transfer*, John Wiley & Sons, New York.
[25] Tien, C.-L., Armaly, B. F., and Jagannathan, P. S., 1969, "Thermal Conductivity of Thin Metallic Films and Wires at Cryogenic Temperatures," *Thermal Conductivity*, Plenum Press, New York, pp. 13–19.
[26] Tien, C.-L., Majumdar, A., and Gerner, F. M., 1998, *Microscale Energy Transport*, Taylor & Francis, Washington, DC.
[27] Nakabeppu, O., Igeta, M., and Inoue, T., 1999, "Microscale Real Temperature Measurement by the AFM Using Thermal Feedback Method," Therm. Sci. Eng., **7**, No. 6, pp. 1–7.